crystals

MDPI

Article

$LiCrO_2$ Under Pressure: In-Situ Structural and Vibrational Studies

Alka B. Garg [1,2,*], Daniel Errandonea [3], Julio Pellicer-Porres [3], Domingo Martinez-Garcia [3], Swayam Kesari [4], Rekha Rao [2,4], Catalin Popescu [5] and Marco Bettinelli [6]

1 High Pressure and Synchrotron Radiation Physics Division, Bhabha Atomic Research Centre, Mumbai 400085, India
2 Homi Bhabha National Institute, Anushaktinagar, Mumbai 400094, India; rekhar@barc.gov.in
3 Departamento de Física Aplicada-ICMUV, MALTA Consolider Team, Universidad de Valencia, Edificio de Investigación, C/Dr. Moliner 50, Burjassot, 46100 Valencia, Spain; Daniel.Errandonea@uv.es (D.E.); Julio.Pellicer@uv.es (J.P.-P.); Domingo.Martinez@uv.es (D.M.-G.)
4 Solid State Physics Division, Bhabha Atomic Research Centre, Mumbai 400085, India; swayam@barc.gov.in
5 CELLS-ALBA Synchrotron Light facility, 08290 Cerdanyola, Barcelona, Spain; cpopescu@cells.es
6 Luminescent Materials Laboratory, Department of Biotechnology, University of Verona and INSTM, UdR Verona, Strada Le Grazie, 15371 34 Verona, Italy; marco.bettinelli@univr.it
* Correspondence: alkagarg@barc.gov.in; Tel.: +91-22-2559-5482

Received: 1 December 2018; Accepted: 17 December 2018; Published: 20 December 2018

Abstract: The high-pressure behaviour of $LiCrO_2$, a compound isostructural to the battery compound $LiCoO_2$, has been investigated by synchrotron-based angle-dispersive X-ray powder diffraction, Raman spectroscopy, and resistance measurements up to 41, 30, and 10 Gpa, respectively. The stability of the layered structured compound on a triangular lattice with *R*-3*m* space group is confirmed in all three measurements up to the highest pressure reached. The dependence of lattice parameters and unit-cell volume with pressure has been determined from the structural refinements of X-ray diffraction patterns that are used to extract the axial compressibilities and bulk modulus by means of Birch–Murnaghan equation-of-state fits. The pressure coefficients for the two Raman-active modes, A_{1g} and E_g, and their mode-Grüneisen parameters are reported. The electrical resistance measurements indicate that pressure has little influence in the resistivity up to 10 GPa. The obtained results for the vibrational and structural properties of $LiCrO_2$ under pressure are in line with the published results of the similar studies on the related compounds. Research work reported in this article contributes significantly to enhance the understanding on the structural and mechanical properties of $LiCrO_2$ and related lithium compounds.

Keywords: high-pressure; X-ray diffraction; Raman spectroscopy; equation of state

1. Introduction

Layered ABO_2 transition-metal oxides, where *A* (*B*) is an alkali or noble metal (3*d* transition metal), have attracted considerable interest due to the wide variety of attributes that are exhibited by them [1–4]. The major crystal structures adopted by these compounds is either delafossite or $\alpha-NaFeO_2$-type structure, which belong to space group *R*-3*m*. In both the structures each element forms a triangular lattice, which follows the stacking arrangement along the *c*-axis in the sequence B^{3+}-O^{2-}-A^{+}-O^{2-}. Difference in the stacking configuration of O^{2-}-A^{+}-O^{2-} layers distinguishes the two crystal structures. The delafossite structure has a straight stacking, while a zigzag stacking is favoured in $\alpha-NaFeO_2$ [5]. The compounds with *A* as noble metal (Cu, Ag, Au) adopt the delafossite structure, forming a family of materials showing a rare combination of electrical conductivity and optical transparency widely known as transparent conducting oxides [6,7]. These compounds find a plethora of technological

functions in devices requiring transparent contacts such as solar cells [8], light-emitting diodes [9], and liquid-crystal displays [10]. On the other hand, compounds with *A* as alkali metal (Li, Na, K) crystallize in the $\alpha-NaFeO_2$ structure. Their study is largely driven by the immense importance of these materials in the electrochemical industry [11–15]. Particularly, the compounds containing lithium have been extensively investigated as cathode materials for lithium-ion batteries, due to their high lithium storage capacity, rate performances, and durability [16]. The first commercialized cathode material, $LiCoO_2$, which is used in the lithium batteries, still dominates the market of portable electronic appliances due to its high volumetric density and excellent lithium intercalation properties [17]. $LiCrO_2$, a compound isostructural to $LiCoO_2$, though, shows a poor reversible lithium intercalation; however, the interest in this compound is due to its multiple electron transfer nature during electrochemical reactions and its large lithium-storage capacity [18]. Furthermore, the addition of a small amount of Cr to many $LiBO_2$ layered materials has shown to induce a drastic enhancement of the electrochemical properties [19]. Reducing the grain size of $LiCrO_2$ also results in the enhancement of the lithium-storage capacity [20,21].

Other than industrially driven research on alkali-metal based compounds, fundamental research on these materials has developed in parallel. The nickelates, chromates, and cobaltates have been the subject of numerous studies, mainly because of their exotic magnetic properties coupled with interesting phase transitions [22–25]. The properties of a material are linked with its crystal structure and they can be tuned by subjecting the material to various thermodynamic variables such as pressure and/or temperature [26]. A few high-pressure studies carried out on delafossite-structured compounds have shown interesting structural behaviour [27–31]. However, the study of the stability of layered $\alpha-NaFeO_2$–type compounds under pressure is sparse. Based upon first-principles calculations, a structural phase transition to a cubic phase was proposed to exist in $LiCoO_2$ at 3 GPa [32]. However, more recent X-ray diffraction, Raman spectroscopic, and theoretical studies show the stability of this compound up to 26 GPa [33]. On the other hand, recent report of high-pressure investigations on lithium titanate has revealed the improved electrical conductivity of the compound under pressure suggesting its possible uses in the future development of lithium batteries [34].

In the case of $LiCrO_2$, after a broad literature search we concluded that the structural stability of $LiCrO_2$ against compression has not been explored so far. In this work, we report the influence of pressure at ambient temperature on the structural, vibrational, and electrical properties of $LiCrO_2$. These properties were investigated by synchrotron X-ray diffraction, Raman spectroscopy, and electrical resistance measurements up to 41, 30, and 10 Gpa, respectively. All three techniques indicate the stability of the ambient crystal structure up to the highest pressure reached in three measurements. The structural details of the ambient rhombohedral phase have been determined at various pressures. The axial compressibility, inter-atomic bond distances, polyhedral compressibility, and isothermal (300 K) P-V equation of state (EOS) of the ambient-pressure phase of $LiCrO_2$ are reported. The pressure dependence of two expected Raman modes, along with their Gruneisen parameter, has been obtained.

2. Experimental Section

2.1. Sample Synthesis and Characterization

Polycrystalline sample of $LiCrO_2$ was prepared by solid state reaction route using high purity Li_2CO_3 and Cr_2O_3 (99.9% purity, Alfa Aesar), taken in 1:1 ratio by weight. The two oxides are meticulously mixed in pestle and mortar, uniaxially compressed into pellets of 13 mm diameter and 5 mm height, and exposed to initial heat treatment at 850 °C for 24 h in programmable resistive furnace, followed by another heating cycle at 1100 °C for 24 h. The resultant product was checked employing X-ray diffraction (angle dispersive mode) using a rotating anode generator with molybdenum target as X-ray source (λ = 0.7107 Å) and Raman spectroscopy (λ = 532 nm laser) for the confirmation of its single phase formation.

$LiCrO_2$ single crystals were grown by the flux method. The growth was started from a mixture of 0.065 mol of Li_2CO_3, 0.014 mol of PbO, 0.034 mol of B_2O_3, and 0.22 mol of Cr_2O_3, which was heated at 1300 °C and then slowly cooled down to 800 °C and subsequently naturally cooled down to room temperature. After separating the crystals from the flux, their crystal structure and purity were confirmed with powder X-ray diffraction (λ = 1.5406 Å).

2.2. High Pressure Measurements

2.2.1. X-ray Diffraction

Powder X-ray diffraction measurements in an Angle-dispersive configuration were carried out at the MSPD-BL04 beamline of the ALBA synchrotron source. A membrane-type diamond-anvil cell (DAC) equipped with 350-μm culet diamonds was used for compressing the sample. Fine particles of the sample with a few Cu grains (to serve as *in-situ* pressure standard [35]) and Ne, as pressure-transmitting medium, were loaded into a sample chamber made from stainless steel metal gasket with a centred hole of 150 μm in diameter. The gasket was previously pre-indented to a thickness of 50 μm. Special care was taken while loading the sample in the sample chamber to reduce the possibility of the sample bridging the diamonds, which may induce unwanted large pressure gradients in the sample [36,37]. X-ray powder patterns at different pressures were collected using monochromatic X-rays (λ = 0.4246 Å) that were focused to 15 × 15 μm^2. Images of the X-ray diffraction rings were recorded on a Rayonix CCD detector. The sample to detector distance, together with the detector orientation and other calibration parameters, were calculated using the diffraction pattern of LaB_6 as standard and the FIT2d software [38]. This software was also used to transform the two-dimensional (2D) diffraction images to one-dimensional (1D) intensity *vs*. two theta diffraction patterns. The structural analysis was performed with GSAS [39].

2.2.2. Raman Spectroscopy

Two independent data sets of Raman measurements at different laboratories were carried out at several pressures. Both the data sets were collected in back-scattering geometry. In first data set, collected up to 15 GPa on the polycrystalline sample, a Mao-Bell-type DAC, with 16:3:1 methanol-ethanol-water mixture (MEW) as pressure-transmitting medium, was employed. The Raman measurements were performed using a 532 nm laser (5 mW). The spectra were collected using a single monochromator coupled with an edge filter and a thermoelectric-cooled Charge Coupled Devices (CCD). The spectral resolution was 3 cm^{-1}. In the second data set collected up to 30 GPa on a single crystal, a membrane-type DAC, with Ne as pressure-transmitting medium was used. Raman spectra were excited using a 632.8 nm laser (10 mW). The experimental setup was home-built using a confocal microscope, an edge filter, a single spectrometer, and a thermoelectric-cooled CCD. The spectral resolution of this setup is better than 2 cm^{-1}. In both sets of measurements, the ruby fluorescence technique [40] was used for in-situ pressure calibration.

2.2.3. Electrical Resistance

Electrical resistance measurements up to a maximum pressure of 10 GPa were made using an opposed Bridgman anvil set-up with 12-mm diameter tungsten carbide anvils [41] that is mounted in a hydraulic press. A pair of pyrophyllite gaskets, with a thickness 200 μm each, and with a central hole of 3 mm in diameter, was employed as the pressure chamber. Steatite was used as a pressure-transmitting medium. Pressure was determined by calibrating the high pressure assembly with the known phase transitions of bismuth. A rectangular piece of the sample cut from the well compacted powdered sample, with 2 mm × 1.5 mm × 0.1 mm in size, was used for resistance (four contacts) measurements [42]. A constant current was applied to the sample by means of the outer leads by using a Keithley current source. The voltage drop was measured using a Keithley nano-voltmeter. The measurements were performed at each pressure with two minutes of pressure stabilization time.

3. Results and Discussion

3.1. Ambient Pressure

As shown in Figure 1, at ambient conditions, the compound adopts the α-$NaFeO_2$-type layered rhombohedral structure that is described by space group *R*-3*m*.

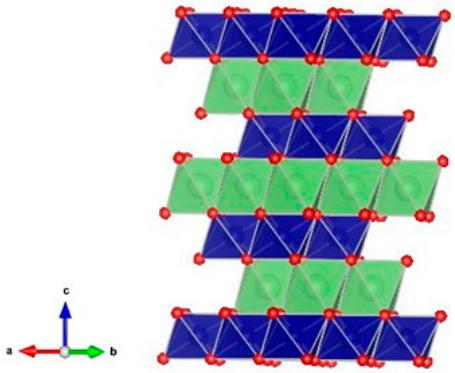

Figure 1. (Colour online) Ambient-pressure crystal structure of the layered structured $LiCrO_2$ (space group *R*-3*m*). Lithium (green) and Chromium (blue) atoms are octahedrally coordinated with oxygen atom (red).

In this structure, the Li atoms are surrounded by edge-sharing oxygen octahedral units, separated by triangular planes of Cr atoms, which makes the compound a two-dimensional (2D) triangular antiferromagnet, isostructural with the common battery material $LiCoO_2$ [43]. Cr atoms are also surrounded by six oxygen atoms. The volume of the lithium octahedron is larger than that of the chromium octahedron. An X-ray diffraction pattern measured at ambient conditions and the Rietveld refinement of the data are shown in Figure 2. All of the observed diffraction peaks could be fitted with the rhombohedral structure (space group *R*-3*m*). This confirms the single phase formation of the compound. The refined lattice parameters are a = 2.8941(3) Å and c = 14.391(3) Å. The corresponding unit-cell volume is V = 104.38(2) $Å^3$, which is in excellent agreement with the value reported in the literature [44].

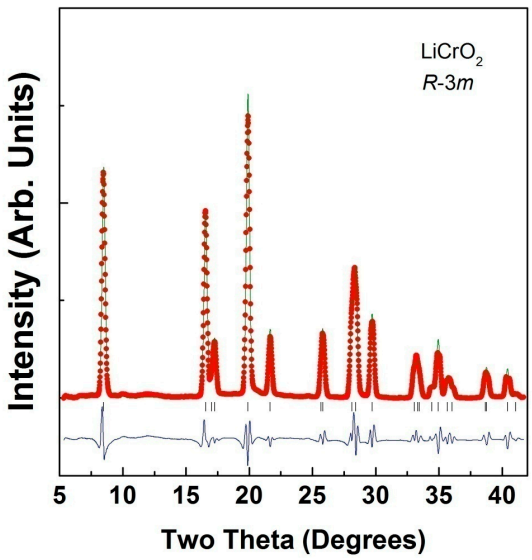

Figure 2. Refined ambient conditions XRD pattern of our $LiCrO_2$ sample. It shows the single phase formation of the compound. Vertical tick marks represent allowed the reflection of the rhombohedral structure with *R*-3*m* space group.

The ambient pressure volume of $LiCrO_2$ is nearly 8% larger than in the isostructural compound $LiCoO_2$. The Wyckoff positions for Li, Cr and oxygen atoms are 3b (0, 0, 0.5), 3a (0, 0, 0), and 6c (0, 0, z), respectively. The only free parameter is the *z* parameter of the oxygen atoms. The refined value is 0.7433(5). R-factors of the refinement are R_p = 4.54% and wR_p = 6.17% (Table 1).

Table 1. Refined structural parameters for $LiCrO_2$ at ambient and high pressures.

Ambient Pressure; a = 2.8941 (3)Å; c = 14.391 (3) Å, R_p = 4.5% and wR_p = 6.2%.				
Atom	**Site**	**x**	**Y**	**Z**
Li	3b	0	0	0.5
Cr	3a	0	0	0
O	6c	0	0	0.7433(4)
Bond length (Å)	Li-O 2.1134	Cr-O 2.0032	Cr-Cr/Li-Li 2.9231	Li-Cr 2.8941
5.3 GPa; a = 2.8736 (3)Å; c = 14.1367 (2) Å, R_p = 2.65% and wR_p = 4.92%				
O	6c	0	0	0.7496 (4)
Bond length (Å)	Li-O 2.0353	Cr-O 2.0288	Cr-Cr/Li-Li 2.8736	Li-Cr 2.8816
16.4 GPa: a = 2.8367 (7) Å; c = 13.753 (5) Å, Rp = 3.85% and wR_P = 5.82%				
O	6c	0	0	0.7662
Bond length (Å)	Li-O 1.8779	Cr-O 2.1316	Cr-Cr/Li-Li 2.8367	Li-Cr 2.8172
21.8 GPa: a = 2.8199 (8) Å; 13.640 (8) Å, Rp = 3.56 % and wR_P = 5.82%				
O	6c	0	0	0.7736 (4)
Bond length (Å)	Li-O 1.8185	Cr-O 2.1828	Cr-Cr/Li-Li 2.8199	Li-Cr 2.7961

Using group-theory analysis, the total irreducible representation for the zone centre optic modes of $LiCrO_2$ is obtained as A_{1g}+ $2A_{2u}$ + E_g + $2E_u$. Among them, two modes (A_{1g} and E_g) are Raman active [45,46]. For the A_{1g} mode, the atomic shift of oxygen atoms is along the *c*-axis, whereas the E_g mode corresponds to vibrations in perpendicular directions. The Raman spectra measured for the polycrystalline sample of $LiCrO_2$ is shown in Figure 3. The two Raman active modes E_g and A_{1g} appear at 456 and 589 cm^{-1}, respectively, and matches well with the previously reported values [46].

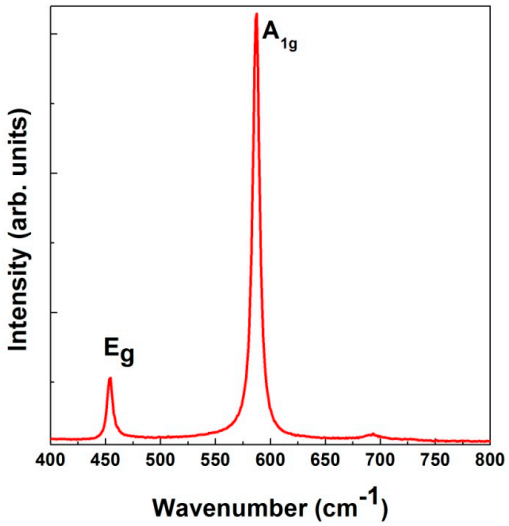

Figure 3. Raman spectrum of as synthesized $LiCrO_2$ at ambient pressure and temperature conditions. The two Raman active modes are clearly observed.

The Raman spectrum did not show any shoulder peaks of the E_g mode, which are usually associated to the presence of Li vacancies in the material [45]. This observation is consistent with the formation of a stoichiometric compound. The experimental reported value of E_g and A_{1g} modes for the isostructural compound $LiCoO_2$ are 486 and 595 cm^{-1} (Table 2) [33]. The two modes in this compound are reported to be predominantly Co-O stretching and O-Co-O bending motions, which are supported by Li isotope substitution experiments as well as a comparison to the isostructural compound $NaCoO_2$. In this compound, the E_g and A_{1g} Raman modes are at 486 and 586 cm^{-1}, respectively [47]. Notice that by substituting sodium for lithium, the E_g mode does not shift in frequency within experimental resolution. On the other hand, the frequency change of the A_{1g} mode is quite small. These two facts prove that in ABO_2 compounds with $NaFeO_2$-type structure, A_{1g} and E_g frequencies depend predominantly on *B* cation. In the case of $LiCrO_2$, the E_g mode has a lower frequency (456 cm^{-1}), which corresponds to a weaker restoring force for vibrations of the chromate units than in the cobaltate units due to the larger ionic radii of Cr^{3+} as compared to the compounds having Co^{3+} at *B* site. In the case of $LiNiO_2$, another isostructural compound with $LiCrO_2$, the E_g and A_{1g} mode frequencies are 465 and 545 cm^{-1}, respectively [48].

Table 2. Experimental Raman modes along with Gruneisen parameters (γ) for a $LiCrO_2$ and isomorphic compounds.

Compounds	*B* Cationic Radii	Raman Mode Assignment	Raman Frequency (ω) (cm^{-1})	Gruneisen Parameter (γ)
[32] $LiCoO_2$	0.545 Å	E_g A_{1g}	486(1) 595(1)	1.15 0.79
[this work] $LiCrO_2$	0.615 Å	E_g A_{1g}	456(2) 589(2)	1.07(2) 1.18(2)
[47] $NaCoO_2$	0.545 Å	E_g A_{1g}	486 586	
[48] $LiNiO_2$	0.56 Å	E_g A_{1g}	465 545	

3.2. High-Pressure Studies

Figure 4 shows the raw 2D image from the CCD detector that was collected at 7.3 GPa. This raw image is representative of the measurement and illustrates the good quality of our data, information which is lost in a standard one dimensional integrated pattern. The evolution of diffraction patterns of $LiCrO_2$ as the pressure is increased is shown in Figure 5a, whereas in Figure 5b a few XRD diffraction patterns collected while pressure unloading is depicted. As marked in the figure, not only the diffraction peaks from $LiCrO_2$ are present. There are also two peaks from the copper used as *in-situ* pressure calibrant. All of the diffraction peaks assigned to the sample are unequivocally indexed with the ambient-pressure rhombohedral structure.

On increasing the pressure, there are no qualitative changes observed in the diffraction patterns. Only shifting of all the peaks to higher angles is found, which is caused by the lattice compression. This evolution of XRD patterns continues until the highest pressure of 41.2 GPa is reached in the present measurements. Similar to $CuAlO_2$ and $CuGaO_2$ delaffosites [30,49], in $LiCrO_2$ also the intensity of the (00k) Bragg peaks and width of the reflections are affected by pressure. However the absence of any extra diffraction peaks indicates the structural stability of the studied material under compression. Refinements of all the diffraction patterns that were collected at various pressures were carried out to obtain the evolution of lattice parameters as a function of pressure. Due to the presence of Cu (111) reflection close to the (104) reflection from the sample, the refinements were carried out by masking these two peaks. Note that Cu being cubic (space group *F*-3*m*), the refinement of a single peak, Cu (200) can be used to determine the pressure. For the diffraction patterns up to 21.8 GPa, a Rietveld refinement was carried out, however, due to texture in the diffraction peaks beyond this pressure, only a profile refinement was carried out above 21.8 GPa. This is sufficient to obtain the correct lattice parameters and cell volume.

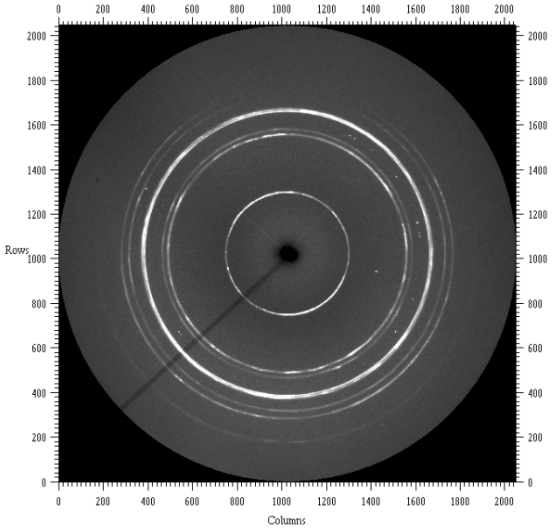

Figure 4. Image of the powder diffraction data of liCrO$_2$ collected at 7.3 GPa on CCD detector.

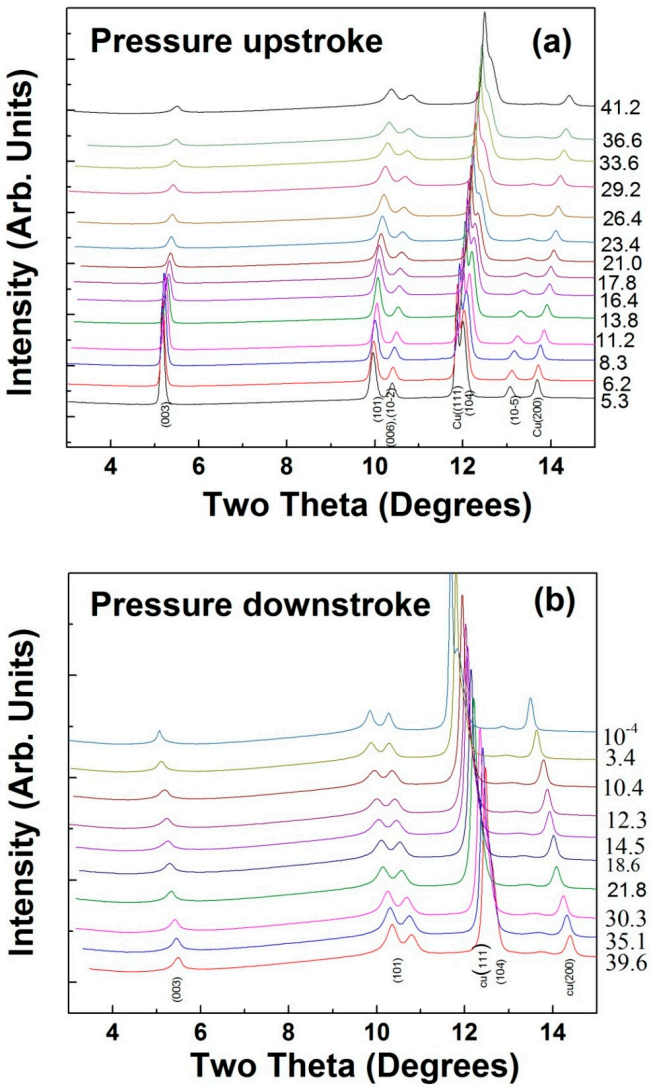

Figure 5. (**a**) Evolution of X-ray diffraction patterns for LiCrO$_2$ while compressing; (**b**) while decompressing. Diffraction peaks from *in-situ* pressure calibrant (Cu) are also indicated. Numbers on the right hand side of y-axis denote the pressure in GPa.

Figure 6a–d show the representative fitted XRD patterns at 5.3, 16.4, 21.7, and 41.2 GPa, respectively.

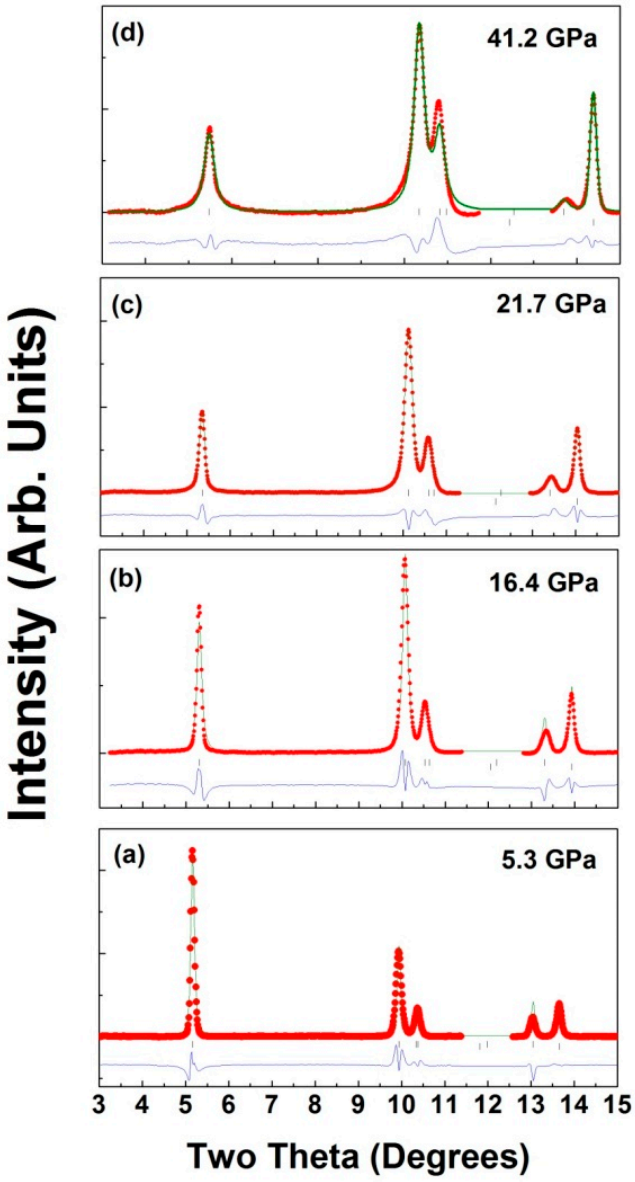

Figure 6. Observed (red), calculated (green), and difference plot (blue) of X-ray powder patterns for $LiCrO_2$ (**a**) at 5.3 GPa, (**b**) 16.4 GPa, (**c**) 21.7 GPa, (**d**) 41.2 GPa. Top and bottom vertical marks indicate Bragg reflections from the sample and pressure calibrant (Cu).

Similar quality of fittings was obtained for all of the pressure points. Structural information at selected pressures and the R-factors of the structural refinements are given in Table 1. Various bond distances are also included in the Table 1. In Figure 7, we present the lattice parameters a and c, and the c/a ratio versus pressure. Error bars in both the axes and the axial ratio have also been plotted along with the determined results. From these data, the isothermal compressibility along the c- and a-axes is estimated to be 5.6×10^{-3} (3×10^{-4}) and 1.24×10^{-3} (4×10^{-5}) GPa^{-1}, respectively. The numbers in the parenthesis represent the estimated error in the fitting. The values of the axial compressibilities indicate a highly anisotropic behaviour of $LiCrO_2$. The c-axis is more than four times as compressible as the a-axis. This behaviour is opposite to the one observed in delafossites, where the c-axis is significantly less compressible than the a-axis. The anisotropic compression that was observed in the axes could be related to the layered framework of the crystal structure. In particular, to the large

compressibility of the Li-O bonds formed between layers of CrO_6 octahedral units as will be discussed in the next section.

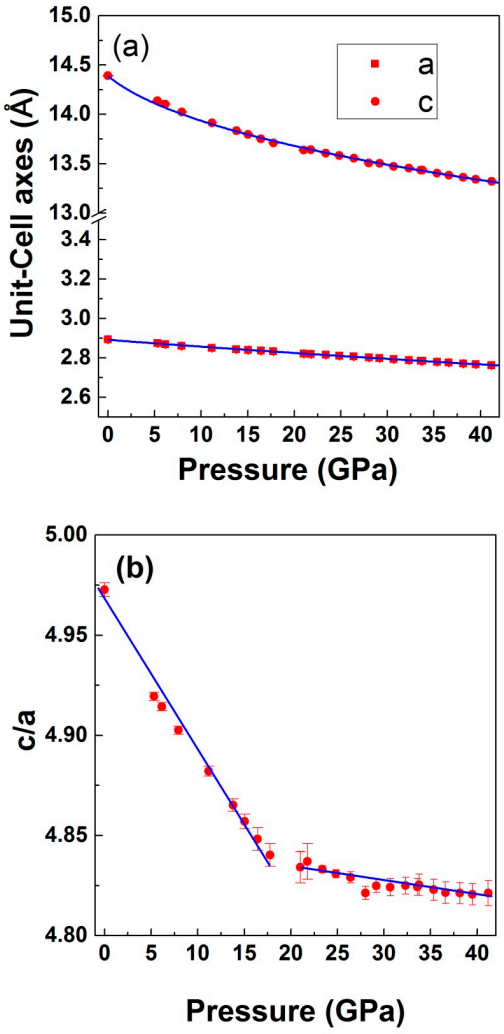

Figure 7. Pressure dependence of (**a**) lattice parameters and (**b**) axial ratio (c/a) of $LiCrO_2$. Symbols present the experimental data points and the solid lines in (**a**) are a Birch–Murnaghan equation of state (BM–EOS) fit to the data. Error bars have also been plotted in the data. A clear slope change in c/a ratio can be seen.

As shown in Figure 1, the structure of $LiCrO_2$ along the *c*-axis can be seen as stacked layers of LiO_6-CrO_6-LiO_6-CrO_6.... octahedral units. At ambient conditions (Figure 1), LiO_6 and CrO_6 polyhedral units are very slightly distorted with two types of bond distances. The average lithium–oxygen bond length (2.113 Å) in the LiO_6 octahedron is 5% larger than the average Cr-O bond length (2.003Å) in the CrO_6 octahedron, with their respective polyhedral volume as 12.51 $Å^3$ and 10.69 $Å^3$. A deeper insight on the influence of pressure on the crystal structure of $LiCrO_2$ can be obtained from a quantitative comparison of the polyhedral compression [50]. In Figure 8, we have plotted the evolution of various bond distances and normalized polyhedral volume of LiO_6 and CrO_6, along with the overall cell volume with pressure.

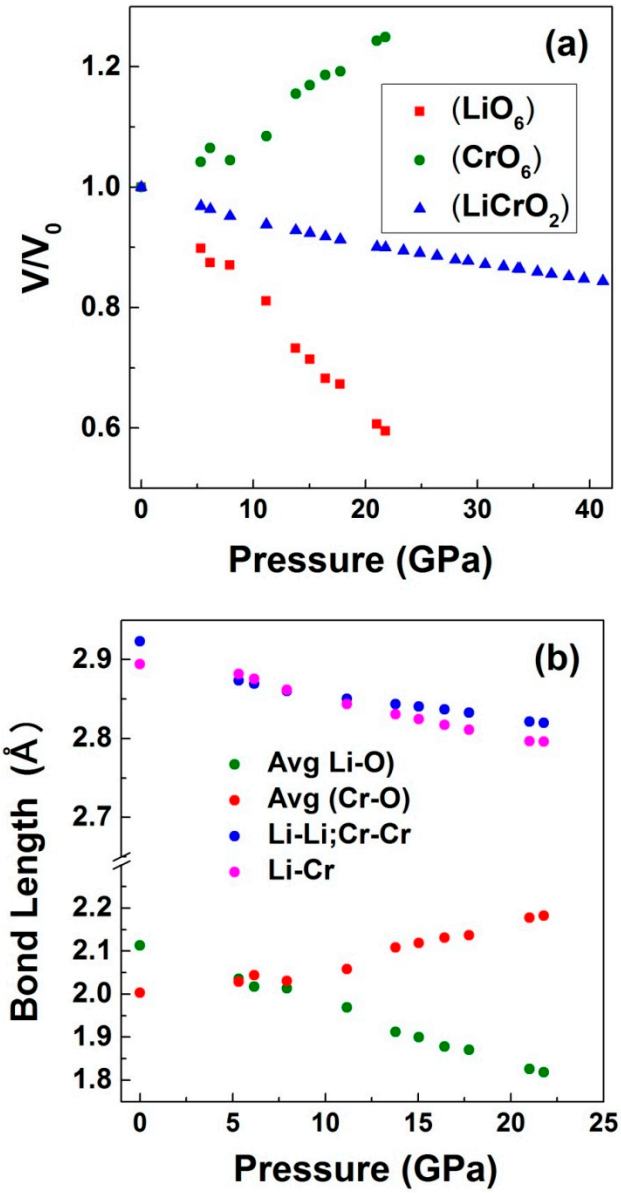

Figure 8. (**a**) Normalized volume of LiO_6 and CrO_6octahedra along with the overall lattice volume. (**b**) Cation-cation and anion-cation bond lengths. Note that except for the Cr-O bond all other bonds shrink with pressure.

The data clearly indicates the compression of LiO_6 polyhedron, whereas the CrO_6 polyhedron expands. However, as can be seen in the figure, the overall effect of pressure on the crystal structure is the reduction of cell volume. The observed phenomenon could be related with the fact that the compressibility of Li-O bonds in α-Li_2O with bulk modulus 75 GPa [51] is much larger when compared to Cr-O bonds in Cr_2O which is having a bulk modulus of 205 GPa [51]. In case of $LiCrO_2$, the compressibility of Li-O bonds is additionally favored by the fact that the Li-O bond length (2.113 Å) is 5% larger than the same bonds in Li_2O (1.996 Å). Consequently, since the position of Li and Cr atoms are fixed by the crystal symmetry, to compress the Li-O bonds, the oxygen atom moves along the *z* direction towards the Li atoms (change of Oz coordinate), resulting in the reduction of LiO_6 unit. Another factor contributing towards the large shrinking of LiO_6 unit could be due to the fact that, under compression, alkali metals (especially lithium) are highly compressible, due to the presence of the *s* electron in its outer shell. As can be seen in the figure, since the oxygen atom is moving towards the lithium, it results in the increase of Cr-O distance. Additionally, Cr being a transition metals,

is quite uncompressible, due to the presence of *d* electrons, therefore it does not contribute enough to the overall compression of CrO_6 units. Since our X-ray diffraction results indicates the absence of any structural phase transition in the compound, in order to retain the ambient crystal-structure symmetry, CrO_6 need to expand, while LiO_6 compresses. In isostructural compound $LiCoO_2$, also, based on Li-O and Co-O bond distances, the highly incompressible behavior of the CoO_6 octahedra has been reported, while it is the LiO_6 octahedra that essentially gets compressed and are responsible for the compressibility of the compound [33]. From our results, we found a change in the axial compressibility beyond 17 GPa, where a clear slope change in c/a ratio is seen (Figure 7). The FWHM of various diffraction peaks along with Cu peaks are shown in Figure 9.

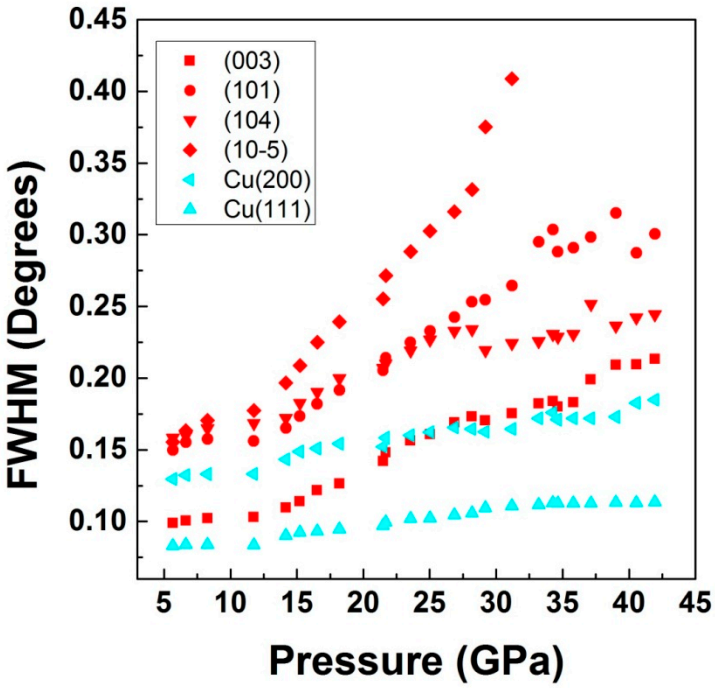

Figure 9. Full-width at half maxima (FWHM) of various diffraction peaks from the sample along with peaks from the pressure calibrant (Cu).

One can clearly see an accelerated broadening of the sample lines beyond 15 GPa while the changes in the width of the Cu peaks are much smaller. It is interesting to mention here that in case of $LiCoO_2$ also the Bragg peaks were reported to broaden beyond 16 GPa which authors have attributed to the presence of non-hydrostaticity due to freezing of nitrogen pressure medium [33]. However, in the same report, the observed broadening of one of the Raman mode beyond 12 GPa was assigned to either anharmonicity or structural effects not detected in diffraction data. In Figure 10, the pressure volume data along with 3rd order Birch–Murnaghan equation of state (BM–EOS) fitted data is shown [52,53]. Notice that the pressure media employed in this study solidify below 10 GPa [36,54], therefore the described phenomena happening around 15 GPa cannot be correlated with the pressure medium solidification and should be intrinsic to $LiCrO_2$ and $LiCoO_2$.

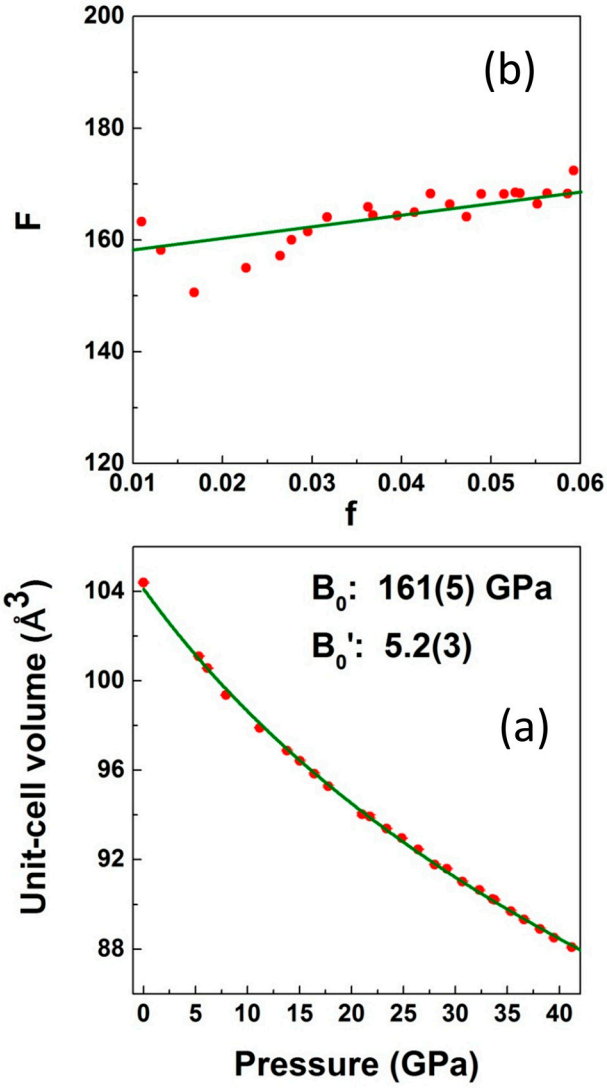

Figure 10. (**a**) Isothermal equations of state data for $LiCrO_2$. Solid squares are experimental data points and solid line is the third order Birch–Murnaghan equation of state fit to the data points. Errors in the volume are smaller than the symbol used. (**b**) Top panel shows the same data converted to F-f plot (see the text).

The fitted bulk modulus (B_0) is 161(5) GPa with a pressure derivative of the bulk modulus (B_0') equal to 5.2(3), which is slightly higher than 149(1) GPa, the experimentally determined bulk modulus for the isostructural compound $LiCoO_2$ (Table 3).

The proper way to analyze the order of BM–EOS needed for fitting the experiment is by means of a transformation of the volume–pressure data into an f–F plot, i.e., Eulerian strain (f) versus normalized stress (F) plot [55]. Such plot gives a direct indication of the compression behavior. If the data points lie on a horizontal line of constant F then a second-order BM–EOS ($B_0' = 4$) is needed to fit the data. If the data points lie on an inclined straight line, the data will be adequately described by a third-order BM–EOS. Positive or negative slopes imply $B_0' > 4$ and $B_0' < 4$, respectively. On the other hand, the intercept on the F axis corresponds to the value of ambient pressure bulk modulus, B_0. From our experiments, a positive slope is obtained, as shown in Figure 10; i.e., the pressure derivative of the bulk modulus is larger than 4, which is indeed consistent with the results that were reported in the previous paragraph. Figure 11a,b show a few representatives Raman spectra of $LiCrO_2$ collected with MEW and Ne as pressure transmitting medium, respectively. The two strong Raman active modes that were observed at ambient pressure could be followed up to the highest pressure in both cases

without any discontinuous changes being observed either in the frequency or relative intensity in the entire pressure region indicating the stability of the compound in the studied pressure range. Both the modes were observed to shift monotonically towards higher frequency indicating the usual pressure hardening of phonons due to bond distance reduction under pressure. It is important to note that we have not observed any change in the Raman mode frequencies corresponding to Cr-O stretching and bending, which could suggest a change in the coordination of Cr from octahedral site to tetrahedral site.

Table 3. Compressibility data of ABO_2 type family of compounds with ordered rock salt structure. LDA and GGA correspond to calculations performed within these approximations. Exp. corresponds to experiments.

Compounds		*a* axis	*c*/*a*	V_0	B_0 (GPa)	B_0'	κ_a (10^{-3} GPa^{-1})	κ_c (10^{-3} GPa^{-1})
[32] $LiCoO_2$	Exp	2.8155	4.992	96.48	149(2)	4.1(3)		
	LDA	2.7921	4.849	91.413	168.5	4.67		
	GGA	2.8559	4.899	98.838	142.9	4.51		
[this work] $LiCrO_2$	Exp	2.8941(3)	4.9725	104.38(2)	161(5)	5.2(3)	1.34	4.78

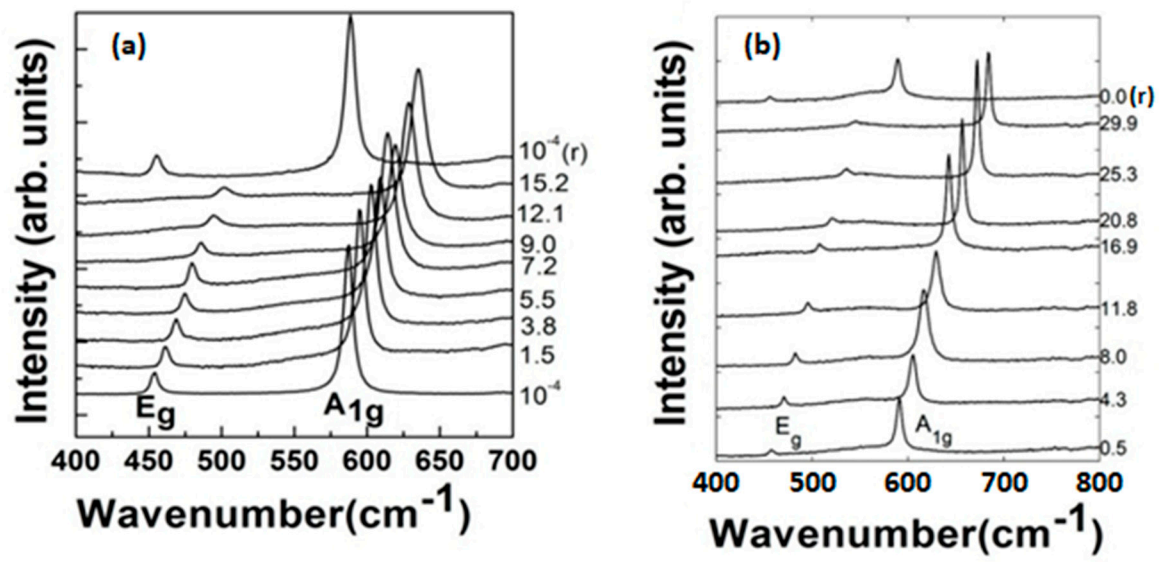

Figure 11. Stacked Raman spectra of $LiCrO_2$ at a few representative pressures (**a**) with methanol-ethanol-water mixture (MEW), (**b**) with Ne. Numbers at the right hand side y-axis are pressure in GPa. Letter r in figures (**a**) and (**b**) indicates pressure released data.

The two independent experiments give consistent results, as can be seen in Figure 12, which shows the pressure dependence of two Raman mode frequencies, which can be expressed as

$$E_g: \omega(P) = 455.9 + 3.5\,P - 0.005P^2$$

$$A_{1g}: \omega(P) = 588.7 + 4.1P - 0.07P^2$$

where ω is the mode frequency in cm^{-1} and P is the pressure in GPa. The modes have been fitted by Lorentzian line shape functions to obtain the peak position.

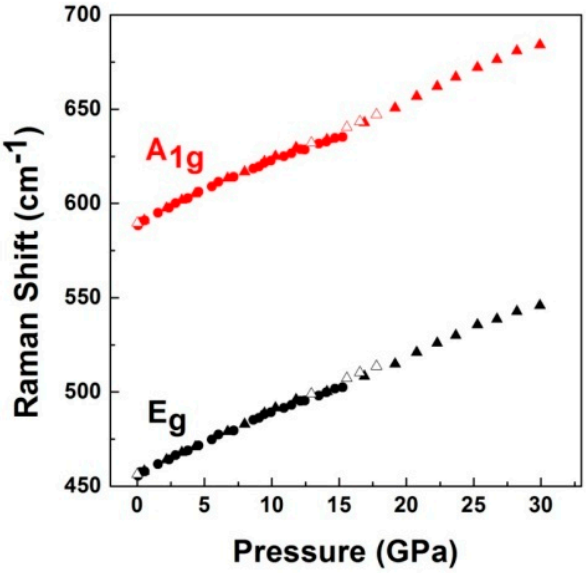

Figure 12. Variation of Raman frequencies shift of $LiCrO_2$ with pressure. Error bars are smaller than the symbol size. Circles denote the data with MEW pressure medium; Solid triangles denote the data with Ne pressure medium. Empty triangles denote the data while unloading with Ne pressure medium.

Note that the quadratic term in the above equations is very small. For the given experimental conditions, the integrated intensity remains nearly same from ambient pressure to 15 GPa. However, we do observe the narrowing down of A_g mode with pressures beyond 15 GPa in the hydrostatic data depicted in Figure 10b. Using this data along with value of zero pressure bulk modulus obtained from the present X-ray diffraction experiments, zero pressure mode Gruneisen parameter which is defined as

$$\gamma = \frac{B_0}{\omega_0}\left(\frac{d\omega}{dP}\right)_{p=0}$$

is calculated and the values for the E_g and A_{1g} mode are 1.07(2) and 1.18(2), respectively. Consequently, the influence of pressure on both modes is very similar. The corresponding values for isostructural compound $LiCoO_2$ are 1.15 and 0.79. The smaller Gruneissen parameter of the E_g modes in $LiCoO_2$ as compared with the other compounds remains an incognita. It is worth mentioning here that $LiCoO_2$ was studied using nitrogen as pressure medium, which remains quasi-hydrostatic only up to 2.4 GPa [56]. This suggests that non-hydrostaticity [41] could have affected the results that were reported for $LiCoO_2$. Future quasi-hydrostatic experiments would be beneficial to clarify this issue. On releasing the pressure completely, the original spectrum is recovered, corroborating the findings from XRD results. The present results highlight the structural stability of the $LiCrO_2$ compound under pressure. In earlier measurements on the similar compound $LiCoO_2$, a significant increase in the integrated intensity of the two modes was reported, which was reversible, ruling out the possibility of pressure induced reorientations of the sample. Those results suggested the possible changes in the electronic structure of the sample. However, in our present measurements on $LiCrO_2$, no significant changes are observed in the integrated intensity of the two modes ruling out the possibility of any major electronic changes in the sample.

To further confirm the absence of any electronic changes induced by pressure in the sample, we carried out electrical resistance measurements on a well compacted sample of $LiCrO_2$ up to 10 GPa. The results are shown in Figure 13.

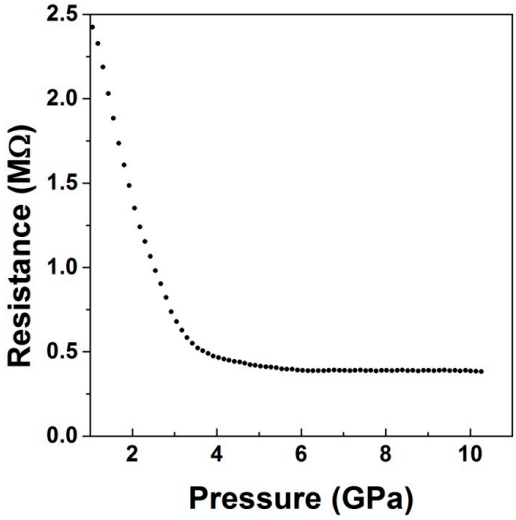

Figure 13. Pressure variation of electrical resistance of $LiCrO_2$. The data indicates absence of structural or electronic transition in the compound.

The initial fall of the resistance up to 3 GPa is typical of measurements in the Bridgman press. Such a phenomenon is usually due to the improvement of the ohmic contact formation between the leads and the sample in the initial stage of compression. On the other hand, the behavior of the resistance beyond 3 GPa corresponds to the intrinsic semiconducting behavior of the sample, which shows a monotonic decrease in the resistance, followed by almost a constant value beyond 4 GPa. This kind of behavior indicates no major pressure-induced changes in the electronic structure of the sample [57]. The behavior of the resistance with pressure therefore confirms that there are no major changes in the electronic structure of $LiCrO_2$ up to 10 GPa.

4. Summary

To summarize, the structural, vibrational, and electronic behavior of $LiCrO_2$ under pressure has been investigated. All three techniques indicate the structural stability of the compound in the pressure range explored. A detailed structural analysis reveals the compression of LiO_6 octahedra, whereas CrO_6 octahedral units expand. However, the overall effect of pressure on the unit cell is the volume reduction. The analysis of the structural data shows an anomaly in the c/a ratio, which is also reflected in the FWHM of the Bragg peaks. The frequency of the two Raman modes of $LiCrO_2$ increases with pressure. The corresponding pressure coefficients and Grüneisen parameters have been determined. On pressure release both X-ray diffraction and Raman data show the reversibility of the sample behavior. The determination of polyhedral and unit-cell compressibilities and the correlation of this information with the study of pressure effects in lattice vibrations is a step forward in extending the understanding of the structural and mechanical properties of $LiCrO_2$. Finally, Raman and resistance measurements suggest that little changes occur in the electronic structure of $LiCrO_2$ under pressure.

Author Contributions: Conceptualization, sample synthesis and data analysis, A.B.G. and D.E; Raman Measurements, R.R, S.K. and J.P.-P.; XRD data collection D.E., J.P.-P., D.M.-G., and C.P.; Single crystal synthesis, M.B. The manuscript is written through contributions of all authors. All authors have given approval to the final version of the manuscript. The authors declare no competing financial interest.

Funding: Three of the authors (D. Errandonea, J. Pellicer-Porres, and D. Martinez-Garcia) are thankful for the financial support to this research from the Spanish Ministerio de Ciencia, Innovación y Universidades, the Spanish Research Agency, and the European Fund for Regional Development under Grant No. MAT2016-75586-C4-1-P and by Generalitat Valencia through the grant Prometeo/2018/123 EFIMAT.

Acknowledgments: XRD experiments were performed at MSPD beamline at ALBA Synchrotron with the collaboration of ALBA staff.

Conflicts of Interest: The authors declare no conflict of interest.

References

1. Mackenzie, A.P. The properties of ultrapure delafossite metals. *Rep. Prog. Phys.* **2017**, *80*, 032501. [CrossRef] [PubMed]
2. Maignan, A.; Martin, C.; Singh, K.; Simon, C.; Lebedev, O.I.; Turner, S. From spin induced ferroelectricity to dipolar glasses: Spinel chromites and mixed delafossites. *J. Solid State Chem.* **2012**, *195*, 41–49. [CrossRef]
3. Julien, C.; Mauger, A.; Zaghib, K.; Groult, H. Optimization of layered cathode materials for lithium-ion batteries. *Materials* **2016**, *9*, 595. [CrossRef]
4. Julien, C. Local cationic environment in lithium nickel–cobalt oxides used as cathode materials for lithium batteries. *Solid State Ionics* **2000**, *136–137*, 887–896. [CrossRef]
5. Seki, S.; Onose, Y.; Tokura, Y. Spin-driven ferroelectricity in triangular lattice antiferromagnets $ACrO_2$ (A = Cu, Ag, Li, or Na). *Phys. Rev. Lett.* **2008**, *101*, 067204. [CrossRef] [PubMed]
6. Sinnarasa, I.; Thimont, Y.; Presmanes, L.; Barnabé, A.; Tailhades, P. Thermoelectric and transport properties of delafossite $CuCrO_2$: Mg thin films prepared by rfmagnetron sputtering. *Nanomaterials* **2017**, *7*, 157. [CrossRef] [PubMed]
7. Walsh, A.; Da Silva, J.L.F.; Wei, S.-H. Multi-component transparent conducting oxides: Progress in materials modelling. *J. Phys. Condens. Matter* **2011**, *23*, 334210. [CrossRef]
8. Yu, M.; Natu, G.; Ji, Z.; Wu, J.Y. P-type dye-sensitized solar cells based on delafossite $CuGaO_2$ nanoplates with saturation photovoltages exceeding 460 mv. *Phys. Chem. Lett.* **2012**, *3*, 1074–1078. [CrossRef]
9. Ling, B.; Zhao, J.L.; Sun, X.W.; Tan, S.T.; Kyaw, A.K.K.; Divayana, Y.; Dong, Z.L. Color tunable light-emitting diodes based on p+-Si/p-$CuAlO_2$/n-ZnO nano rod array hetero junctions. *Appl. Phys. Lett.* **2010**, *97*. [CrossRef]
10. Chae, G.S.A. Modified transparent conducting oxide for flat panel displays only. *Jpn. J. Appl. Phys. Part 1* **2001**, *40*, 3A. [CrossRef]
11. Komaba, S.; Takei, C.; Nakayama, T.; Ogata, A.; Yabuuchi, N. Electrochemical intercalation activity of layered $NaCrO_2$ vs. $LiCrO_2$. *Electrochem. Commun.* **2010**, *12*, 355–358. [CrossRef]
12. Chen, C.-Y.; Matsumoto, K.; Nohira, T.; Hagiwara, R.; Fukunag, A.; Sakai, S.; Nitta, K.; Inazawa, S. Electrochemical and structural investigation of $NaCrO_2$ as a positive electrode for sodium secondary battery using inorganic ionic liquid NaFSA–KFSA. *J. Power Sources* **2013**, *237*, 52–57. [CrossRef]
13. Hou, P.; Chu, G.; Gao, J.; Zhang, Y.; Zhang, L. Li-ion batteries: Phase transition. *Chin. Phys. B* **2016**, *25*, 016104. [CrossRef]
14. Song, H.-K.; Lee, K.T.; Kim, M.G.; Nazar, L.F.; Cho, J. Recent progress in nanostructured cathode materials for lithium secondary batteries. *Adv. Funct. Mater.* **2010**, *20*, 3818–3834. [CrossRef]
15. Kalluri, S.; Yoon, M.; Jo, M.; Park, S.; Myeong, S.; Kim, J.; Dou, S.X.; Guo, Z.; Cho, J. Li-ion cells: Surface engineering strategies of layered $LiCoO_2$ cathode material to realize high-energy and high-voltage Li-ion cells. *Adv. Energy Mater.* **2017**, *7*, 1601507–1601521. [CrossRef]
16. Cao, Q.; Zhang, H.P.; Wang, G.J.; Xia, Q.; Wu, Y.P.; Wu, H.Q. A novel carbon-coated $LiCoO_2$, as cathode material for lithium ion battery. *Electrochem. Commun.* **2007**, *9*, 1228–1232. [CrossRef]
17. Mizushima, K.; Jones, P.C.; Wiseman, P.J.; Goodenough, J.B. Li_xCoO_2 ($0 < x < -1$): A new cathode materialforbatteries of high energy density. *Mater. Res. Bull.* **1980**, *15*, 783–789.
18. Lyu, Y.; Ben, L.; Sun, Y.; Tang, D.; Xu, K.; Gu, L.; Xiao, R.; Li, H.; Chen, L.; Huang, X. Atomic insight into electrochemical inactivity of lithium chromate ($LiCrO_2$): Irreversible migration of chromium into lithium layers in surface regions. *J. Power Sources* **2015**, *273*, 1218–1225. [CrossRef]
19. Pan, C.; Lee, Y.J.; Ammundsen, B.; Grey, C.P. ^{6}Li MAS NMR studies of the local structure and electrochemical properties of Cr-doped lithium manganese and lithium cobalt oxide cathode materials for lithium-ion batteries. *Chem. Mater.* **2002**, *14*, 2289–2299. [CrossRef]
20. Tang, W.; Liu, L.L.; Tian, S.; Li, L.; Yue, Y.B.; Wu, Y.P.; Guan, S.Y.; Zhu, K. Nano-$LiCoO_2$ as cathode material of large capacity and high rate capability for aqueous rechargeable lithium batteries. *Electrochem. Commun.* **2010**, *12*, 1524–1526. [CrossRef]
21. Lyu, Y.; Liu, Y.; Gu, L. Surface structure evolution of cathode materials for Li-ion batteries. *Chin. Phys. B* **2016**, *25*, 018209. [CrossRef]
22. Olariu, A.; Mendels, P.; Bert, F.; Ueland, B.G.; Schiffer, P.; Berger, R.F.; Cava, R.J. Unconventional dynamics in triangular Heisenberg antiferromagnet NaCrO. *Phys. Rev. Lett.* **2006**, *97*, 167203. [CrossRef] [PubMed]

23. Kemp, J.P.; Cox, P.A.; Hodby, J.W. Magnetic susceptibility studies of $LiNiO_2$ and $NaNiO_2$. *J. Phys. Condens. Matter* **1990**, *2*, 31. [CrossRef]
24. de Brion, S.; Bonda, M.; Darie, C.; Bordet, P.; Sheikin, I. Magnetic phase diagram of the S = 1/2 triangular layered compound $NaNiO_2$: A single crystal study. *J. Phys. Condens. Matter* **2010**, *22*, 126001. [CrossRef] [PubMed]
25. Soubeyroux, J.L.; Fruchart, D.; Delmas, C.; Le Flem, G. Neutron powder diffraction studies of two-dimensional magnetic oxides. *J. Magn. Magn. Mater.* **1979**, *14*, 159–162. [CrossRef]
26. Bandiello, E.; Errandonea, D.; Pellicer-Porres, J.; Garg, A.B.; Rodriguez-Hernandez, P.; Muñoz, A.; Martinez-Garcia, D.; Rao, R.; Popescu, C. Effect of High Pressure on the Crystal Structure and Vibrational Properties of Olivine-Type $LiNiPO_4$. *Inorg. Chem.* **2018**, *57*, 10265–10276. [CrossRef] [PubMed]
27. Garg, A.B.; Mishra, A.K.; Pandey, K.K.; Sharma, S.M. Multiferroic $CuCrO_2$ under high pressure: In situ X-ray diffraction and Raman spectroscopic studies. *J. Appl. Phys.* **2014**, *116*, 133514. [CrossRef]
28. Salke, N.P.; Garg, A.B.; Rao, R.; Achary, S.N.; Gupta, M.K.; Mittal, R.; Tyagi, A.K. Phase transitions in delafossite $CuLaO_2$ at high pressures. *J. Appl. Phys.* **2014**, *115*, 133507. [CrossRef]
29. Pellicer-Porres, J.; Segura, A.; Martinez, E.; Saitta, A.M.; Polian, A.; Chervin, J.C.; Canny, B. Vibrational properties of delafossite $CuGaO_2$ at ambient and high pressures. *Phys. Rev. B* **2005**, *72*, 064301. [CrossRef]
30. Pellicer-Porres, J.; Segura, A.; Ferrer-Roca, C.; Polian, A.; Munsch, P.; Kim, D. XRD and XAS structural study of $CuAlO_2$ under high pressure. *J. Phys. Condens. Mater.* **2013**, *25*, 115406. [CrossRef]
31. Garg, A.B.; Rao, R. Copper Delafossites under High Pressure—A Brief Review of XRD and Raman Spectroscopic Studies. *Crystals* **2018**, *8*, 255. [CrossRef]
32. Wolverton, C.; Zunger, A. Prediction of Li intercalation and battery voltages in layered vs. cubic $LixCoO_2$. *J. Electrochem. Soc.* **1998**, *145*, 2424–2431. [CrossRef]
33. Wang, X.; Loa, I.; Kunc, K.; Syassen, K.; Amboage, M. Effect of pressure on the structural properties and Raman modes of $LiCoO_2$. *Phys. Rev. B* **2005**, *72*, 224102. [CrossRef]
34. Huang, Y.; He, Y.; Sheng, H.; Lu, X.; Dong, H.; Samanta, S.; Dong, H.; Li, X.; Kim, D.Y.; Mao, H.-K.; et al. Li-ion battery material under high pressure: Amorphization and enhanced conductivity of $Li_4Ti_5O_{12}$. *Natl. Sci. Rev.* **2018**. [CrossRef]
35. Dewaele, A.; Loubeyre, P.; Mezouar, M. Equations of state of six metals above 94 GPa. *Phys. Rev. B* **2004**, *70*, 094112. [CrossRef]
36. Garg, A.B.; Errandonea, D.; Rodríguez-Hernández, P.; López-Moreno, S.; Muñoz, A.; Popescu, C. High-pressure structural behaviour of $HoVO_4$: Combined XRD experiments and ab-initio calculations. *J. Phys. Condens. Matter* **2014**, *26*, 265402. [CrossRef] [PubMed]
37. Garg, A.B.; Errandonea, D.; Rodríguez-Hernández, P.; Muñoz, A. $ScVO_4$ under non-hydrostatic compression: A new metastable polymorph. *J. Phys. Condens. Matter* **2017**, *29*, 055401. [CrossRef] [PubMed]
38. Hammersley, A.P.; Svensson, S.O.; Hanfland, M.; Fitch, A.N.; Häusermann, D. Two-dimensional detector software: From real detector to idealised image or two-theta scan. *High Pressure Res.* **1996**, *14*, 235–248. [CrossRef]
39. Larson, A.C.; von Dreele, R.B. *General Structure Analysis System*; LANL Report; Los Alamos National Laboratory: Los Alamos, NM, USA, 2004; pp. 86–748.
40. Syassen, K. Ruby under pressure. *High Press. Res.* **2008**, *28*, 75–126. [CrossRef]
41. Garg, A.B.; Verma, A.K.; Vijayakumar, V.; Rao, R.S.; Godwal, B.K. High-pressure experimental and theoretical investigations on the fluorite structured compound $AuAl_2$. *Phys. Rev. B* **2005**, *72*, 024112. [CrossRef]
42. Errandonea, D.; Segura, A.; Martínez-García, D.; Muñoz-San Jose, V. Hall-effect and resistivity measurements in CdTe and ZnTe at high pressure: Electronic structure of impurities in the zinc-blende phase and the semimetallic or metallic character of the high-pressure phases. *Phys. Rev. B* **2009**, *79*, 125203. [CrossRef]
43. Chen, H.; Freeman, C.L.; Harding, J.H. Charge disproportionation and Jahn-Teller distortion in $LiNiO_2$ and $NaNiO_2$: A density functional theory study. *Phys. Rev. B* **2011**, *84*, 085108. [CrossRef]
44. Soubeyroux, J.L.; Fruchart, D.; Marmeggi, J.C.; Fitzgerald, W.J.; Delmas, C.; Le Flem, G. Structure magnetique de $LiCrO_2$. *Phys. Status Solidi A* **1981**, *67*, 633–642. [CrossRef]
45. Inaba, M.; Iriyama, Y.; Ogumi, Z.; Todzuka, Y.; Tasaka, A. Raman study of layered rock-salt $LiCoO_2$ and its electrochemical lithium deintercalation. *J. Raman Spectrosc.* **1997**, *28*, 613–617. [CrossRef]

46. Suzuki, M.; Yamada, I.; Kadowaki, H.; Takei, F. A Raman scattering investigation of the magnetic ordering in the two-dimensional triangular lattice antiferromagnet $LiCrO_2$. *J. Phys. Condens. Matter* **1993**, *5*, 4225. [CrossRef]
47. Yang, H.X.; Xia, Y.; Shi, Y.G.; Tian, H.F.; Xiao, R.J.; Liu, X.; Liu, Y.L.; Li, J.Q. Raman spectroscopy study of α-,β-,γ-Na_xCoO_2 and γ-$(Ca,Sr)_xCoO_2$. *Phys. Rev. B* **2006**, *74*, 094301. [CrossRef]
48. Kalyani, P.; Kalaiselvi, N. Various aspects of $LiNiO_2$ chemistry: *A review*. *Sci. Technol. Adv. Mater.* **2005**, *6*, 689–703. [CrossRef]
49. Pellicer-Porres, J.; Segura, A.; Ferrer-Roca, C.; Martínez-García, D.; Sans, J.A.; Martínez, E.; Itié, J.P.; Polian, A.; Baudelet, F.; Muñoz, A.; et al. Structural evolution of the $CuGaO_2$ delafossite under high pressure. *Phys. Rev. B* **2004**, *69*, 024109. [CrossRef]
50. Gomis, O.; Lavina, B.; Rodriguez-Hernandez, P.; Muñoz, A.; Errandonea, R.; Errandonea, D.; Bettinelli, M. High-pressure structural, elastic, and thermodynamic properties of zircon-type $HoPO_4$ and $TmPO_4$. *J. Phys.: Condens. Matter* **2017**, *29*, 095401.
51. Lazicki, A.; Yoo, C.-S.; Evans, W.J.; Pickett, W.E. Pressure-induced antifluorite-to-anticotunnite phase transition in lithium oxide. *Phys. Rev. B* **2006**, *73*, 184120. [CrossRef]
52. Dymshits, A.M.; Dorogokupets, P.I.; Sharygin, I.S.; Litasov, K.D.; Shatskiy, A.; Rashchenko, S.V.; Ohtani, E.; Suzuki, A.; Higo, Y. Thermoelastic properties of chromium oxide Cr_2O_3 (eskolaite) at high pressures and temperature. *Phys. Chem. Miner.* **2016**, *43*, 447–458. [CrossRef]
53. Birch, F. Elasticity and constitution of the Earth's interior. *J. Geophys. Res.* **1952**, *57*, 227–286. [CrossRef]
54. Errandonea, D.; Meng, Y.; Somayazulu, M.; Hausermann, D. Pressure induced alpha-omega transition in titanium metal: A systematic study of the effects of uniaxial stress. *Physica B* **2005**, *355*, 116. [CrossRef]
55. Heinz, D.L.; Jeanloz, R. The equation of state of the gold calibration standard. *J. Appl. Phys.* **1984**, *55*, 885. [CrossRef]
56. Angel, R.J.; Bujak, M.; Zhao, J.; Gatta, G.D.; Jacobsen, S.D. Effective hydrostatic limits of pressure media for high-pressure crystallographic studies. *J. Appl. Cryst.* **2007**, *40*, 26–32. [CrossRef]
57. Errandonea, D.; Muñoz, A.; Gonzalez-Platas, J. Comment on "High-pressure X-ray diffraction study of YBO_3/Eu^{3+}, $GdBO_3$, and $EuBO_3$: Pressure-induced amorphization in $GdBO_3$". *J. Appl. Phys.* **2014**, *115*, 216101. [CrossRef]